Half-life measurements in ^{164,166}Dy using γ-γ fast-timing spectroscopy with the ν-Ball spectrometer

R. L. Canavan,[1,2,*] M. Rudigier,[1,3] P. H. Regan,[1,2] M. Lebois,[4,5] J. N. Wilson,[4,5] N. Jovancevic,[4,5] P.-A. Söderström,[6] S. M. Collins,[1,2] D. Thisse,[4,5] J. Benito,[7] S. Bottoni,[8] M. Brunet,[1] N. Cieplicka-Oryńczak,[9] S. Courtin,[10] D. T. Doherty,[1] L. M. Fraile,[7] K. Hadyńska-Klęk,[1,11] G. Häfner,[12,13] M. Heine,[10] Ł. W. Iskra,[8,9] V. Karayonchev,[13] A. Kennington,[1] P. Koseoglou,[3,14] G. Lotay,[1] G. Lorusso,[1,2] M. Nakhostin,[1] C. R. Niţă,[15] S. Oberstedt,[16] Zs. Podolyák,[1] L. Qi,[4,5] J.-M. Régis,[13] V. Sánchez-Tembleque,[7] R. Shearman,[2] V. Vedia,[7] and W. Witt[3,14]

[1]*Department of Physics, University of Surrey, Guildford GU2 7XH, United Kingdom*
[2]*National Physical Laboratory, Teddington, Middlesex TW11 0LW, United Kingdom*
[3]*Institut für Kernphysik, Technische Universität Darmstadt, Schlossgartenstrasse 9, 64289 Darmstadt, Germany*
[4]*IPN Orsay, 15 Rue G. Clémenceau, 91406 Orsay Cedex, France*
[5]*Université Paris-Saclay, 15 Rue G. Clémenceau, 91406 Orsay Cedex, France*
[6]*Extreme Light Infrastructure - Nuclear Physics (ELI-NP), Strada Reactorului 30, Măgurele 077126, Romania*
[7]*Grupo de Física Nuclear & IPARCOS, Universidad Complutense de Madrid, CEI Moncloa, 28040 Madrid, Spain*
[8]*Dipartimento di Fisica, Universitá degli Studi di Milano and INFN Sezione Milano, I-20133 Milano, Italy*
[9]*Institute of Nuclear Physics, Polish Academy of Sciences, PL-31-342 Kraków, Poland*
[10]*IPHC and CNRS, Université de Strasbourg, F-67037 Strasbourg, France*
[11]*Faculty of Physics, University of Warsaw, PL 02-093, Warsaw, Poland*
[12]*CSNSM, CNRS/IN2P3, Université Paris-Saclay, F-91405 Orsay, France*
[13]*Institut für Kernphysik der Universität zu Köln, Zülpicher Strasse 14 77, D-50937 Köln, Germany*
[14]*GSI Helmholtzzentrum für Schwerionenforschung GmbH, 64291 Darmstadt, Germany*
[15]*Horia Hulubei National Institute of Physics and Nuclear Engineering (IFIN-HH), R-077125 Bucharest, Romania*
[16]*European Commission, Joint Research Centre, Directorate G, Retieseweg 111, 2440 Geel, Belgium*

(Received 26 September 2019; revised manuscript received 3 January 2020; accepted 6 February 2020; published 26 February 2020)

We report on the measurement of lifetimes of excited states in the near-mid-shell nuclei ^{164,166}Dy using the gamma-ray coincidence fast-timing method. The nuclei of interest were populated using reactions between an ^{18}O beam and a gold-backed isotopically enriched ^{164}Dy target of thickness 6.3 mg/cm^2 at primary beam energies of 71, 76, and 80 MeV from the IPN-Orsay laboratory, France. Excited states were populated in ^{164}Dy, ^{166}Dy, and ^{178,179}W following Coulomb excitation, inelastic nuclear scattering, two-neutron transfer, and fusion-evaporation reaction channels respectively. Gamma rays from excited states were measured using the ν-Ball high-purity germanium (HPGe)-$LaBr_3$ hybrid γ-ray spectrometer with the excited state lifetimes extracted using the fast-timing coincidence method using HPGe-gated $LaBr_3$-$LaBr_3$ triple coincident events. The lifetime of the first $I^\pi = 2^+$ excited state in ^{166}Dy was used to determine the transition quadrupole deformation of this neutron-rich nucleus for the first time. The experimental methodology was validated by showing consistency with previously determined excited state lifetimes in ^{164}Dy. The half-lives of the yrast 2^+ states in ^{164}Dy and ^{166}Dy were 2.35(6) and 2.3(2) ns, respectively, corresponding to transition quadrupole moment values of $Q_0 = 7.58(9)$ and 7.5(4) eb, respectively. The lifetime of the yrast 2^+ state in ^{166}Dy is consistent with a quenching of nuclear quadrupole deformation at $\beta \approx 0.35$ as the $N = 104$ mid-shell is approached.

DOI: 10.1103/PhysRevC.101.024313

I. INTRODUCTION

The study of nuclear structure in deformed nuclei away from sphericity is important in achieving a complete understanding of the nuclear many-body problem. It is well established that nuclear quadrupole collectivity increases with the valence-proton (N_π), valence-neutron (N_ν) product [1]. However, for rare-earth nuclei near $N = 102$–106, microscopic effects cause a saturation of the $B(E2)$ values a few nucleons below the mid-shell at $N = 104$ [2,3]. The current work aims to establish the lifetime of the first 2^+ excited state in ^{166}Dy to track the evolution of the quadrupole deformation across the Dy isotopic chain, towards the ^{170}Dy$_{104}$ mid-shell. ^{170}Dy is a double mid-shell nucleus with the largest number of valence nucleons below the doubly magic $^{208}_{82}$Pb$_{126}$ [4]. However, the consideration of only the number of valence nucleons cannot explain the energy systematics in the vicinity of ^{170}Dy, possibly due to the presence of deformed and spherical subshell closures, similar to those suggested for the

*Corresponding author: r.canavan@surrey.ac.uk

Sm and Gd nuclei along the $N = 100$ isotonic chain [5,6]. Microscopic theoretical studies predict that along the isotope chain the maximum quadrupole deformation occurs below the $N = 104$ mid-shell [7,8].

To date, there are no experimental measurements of the yrast 2^+ lifetimes in any of the neutron-rich even-even Dy isotopes with $A > 164$, the last stable isotope of this element. Existing studies for the neutron-rich nuclei report only on the energies of excited states and ground-state decay lifetimes within the nuclei [9–15]. The focus of the current work is to measure the lifetime of the first 2^+ state in ^{166}Dy and to determine the $B(E2)\downarrow = B(E2 : 2_1^+ \rightarrow 0_{g.s.}^+)$ reduced transition strength for ^{166}Dy and the corresponding β_2 deformation parameter, for the first time in a neutron-rich Dy isotope. The production of the ^{166}Dy nucleus is also of interest due to its use as an *in vivo* generator for the radiopharmaceutical ^{166}Ho, which is used for radiotherapy [16,17], with the ^{166}Dy mother produced via sequential two-neutron capture on ^{164}Dy.

II. EXPERIMENTAL DETAILS AND REACTION CHANNEL SELECTION

The states of interest in ^{166}Dy were populated at an experiment carried out using the accelerator at the ALTO facility at the IPN Orsay. A pulsed ^{18}O beam was provided at three separate primary energies of 71, 76, and 80 MeV, each with a pulse duration of 2 ns and a period of 400 ns, and an average current of 35 *e*nA charge state $Q = 6^+$. A ^{164}Dy target of 6.3 mg/cm^2 and 95% isotopic enrichment was used with 1 mg/cm^2 Au backing. The nominal fusion-Coulomb barrier for this reaction, in the laboratory frame, is approximately 71 MeV. The desired reaction was via ^{164}Dy(^{18}O, ^{16}O) ^{166}Dy. The production of this channel was significantly suppressed relative to the main reaction channels (with cross sections approximately 10^3 times stronger than the $2n$ transfer) from the Coulomb excitation by inelastic scattering on the ^{164}Dy target nucleus, and the ^{164}Dy(^{18}O, 4n) ^{178}W fusion evaporation reaction (a more detailed study of ^{178}W from this experiment can be found in [18]).

To detect the γ rays produced, the ν-Ball hybrid γ-ray detector array containing 24 high-purity germanium (HPGe) clover detectors, 10 coaxial HPGe detectors, and 20 $LaBr_3$ detectors was used [19–21]. All of the HPGe detectors were shielded against Compton scattering using bismuth germanate (BGO) scintillators. The HPGe detectors and BGO shields were were able to see radiation coming from the target position and could be used for calorimetry purposes. The timing signals from the array were obtained using digitizers and the software of the FASTER system, developed by LPC Caen, France [19,21]. For the $LaBr_3$ scintillators a digital CFD (constant-fraction discriminator) algorithm, which evaluates a second order polynomial to interpolate the zero crossing of the discriminator signal, was used by the QDC-TDC (charge-to-digital converter and time-to-digital converter) module to achieve subnanosecond time precision, with the capability of 7.8 ps LSB (least significant bit) accuracy [19,21]. The data were acquired with a trigger in place, so events were accepted when at least one $LaBr_3$ and one HPGe, or, two $LaBr_3$ detectors, were hit within 2 μs.

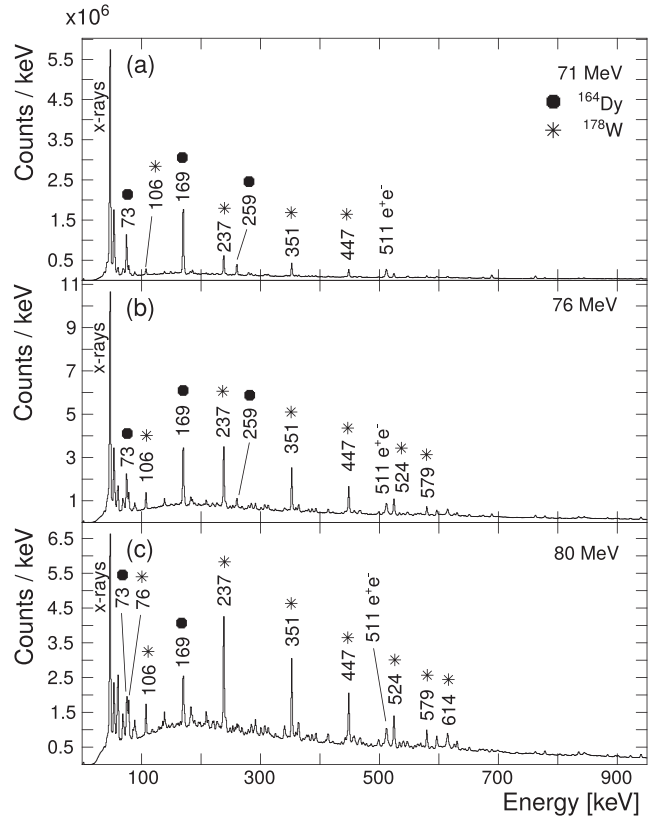

FIG. 1. Total energy spectrum at beam energies 71, 76, and 80 MeV, in panels (a)–(c), respectively, for events containing at least one γ ray detected by a Compton suppressed HPGe detector.

Figure 1 shows the total energy spectra for events which contain at least one clean HPGe γ ray (not vetoed by Compton suppression), from the three beam energies. The experiment was run at 71, 76, and 80 MeV for ≈22, ≈60, and ≈48 hours, respectively.

The event total energy and multiplicity (number of detectors fired) were exploited to improve the reaction channel selection in the current work. The three main reactions produced ^{164}Dy, ^{166}Dy, and ^{178}W via different reaction mechanisms, each of which has its own distribution of total event energy (E) and total event multiplicity (N). These quantities are defined as follows: $E = E(\text{HPGe}) + E(\text{LaBr}_3) + E(\text{BGO})$ and $N = n\text{HPGe} + n\text{LaBr}_3 + n\text{BGO}$, where nHPGe is the HPGe detector multiplicity after add-back and Compton suppression, $n\text{LaBr}_3$ is the $LaBr_3$ detector multiplicity, and nBGO is the BGO multiplicity in events which were not Compton vetoed. The γ rays, which contribute to the event energy and multiplicity, are those that have not been Compton vetoed, and which are detected within the 2 μs coincidence window of each event.

Figure 2 shows the effectiveness of N and E gates to select a particular reaction channel. HPGe γ-γ matrices were created with the constraint that at least two HPGe detectors

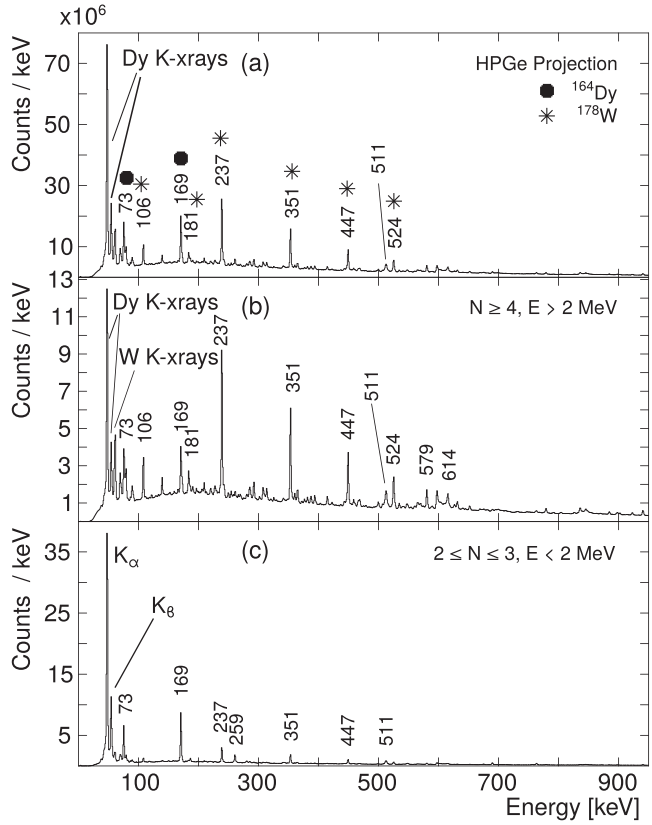

FIG. 2. (a) Projection of prompt HPGe-HPGe coincidence matrix. (b) Projection of prompt HPGe-HPGe matrix with $N \geqslant 4$ and $E > 2$ MeV, enhancing fusion evaporation events from ^{178}W. (c) Projection of prompt HPGe-HPGe matrix with $2 \leqslant N \leqslant 3$ and $E < 2$ MeV, enhancing events from Coulomb excitation by inelastic excitation of the ^{164}Dy target nucleus. These data were taken at a beam energy of 76 MeV.

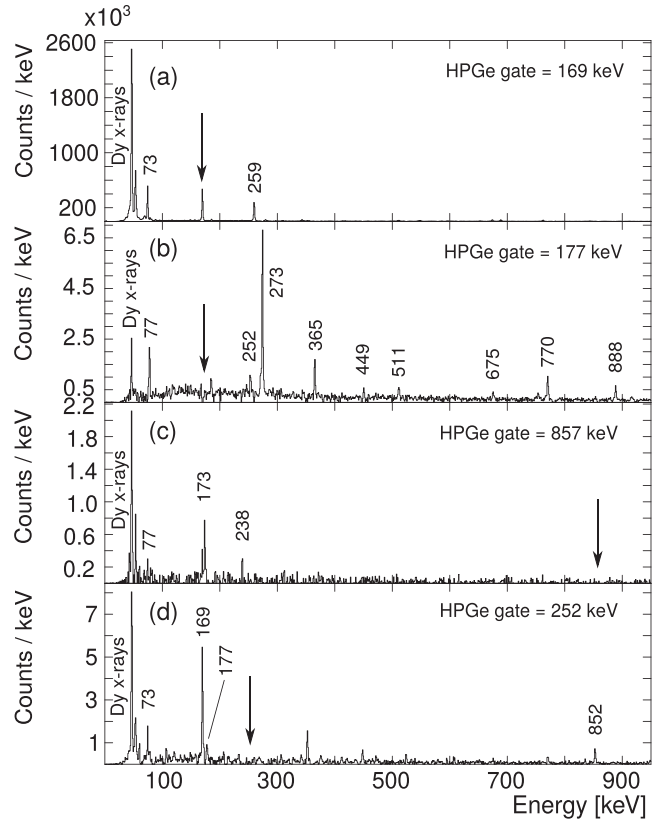

FIG. 3. Projections from a prompt HPGe-HPGe coincidence matrix, with $N \leqslant 4$ for the 2 μs event, after applying background-subtracted HPGe gates on transitions in ^{164}Dy [panel (a)] and ^{166}Dy [panels (b)–(d)]. Arrows indicate the energies where gates were set. These data were taken at a beam energy of 76 MeV.

fired ±50 ns of the beam pulse, within the 2 μs event window. Additional constraints were placed on some of the matrices to preferentially select either fusion evaporation or Coulomb excitation events. Plot (a) gives the projection of the prompt HPGe-HPGe matrix, with no additional constraints, at 76 MeV beam energy. Plot (b) has $N \geqslant 4$ and $E > 2$ MeV constraints to select transitions originating from ^{178}W. Plot (c) has $2 \leqslant N \leqslant 3$ and $E < 2$ MeV constraints to pick out transitions originating from ^{164}Dy.

Figure 3 demonstrates the ability to separate the ^{164}Dy and ^{166}Dy nuclei using background-subtracted HPGe energy gates; in addition it justifies the level scheme of ^{166}Dy discussed in the next section. The plots are created from a prompt HPGe-HPGe coincidence matrix using the data taken at 76 MeV beam energy, where at least two HPGe detectors fired ±50 ns of the beam pulse and the 2 μs event window contained $N \leqslant 4$. Plot (a) shows the HPGe spectrum after gating on the yrast $4^+ \rightarrow 2^+$ transition at 169 keV in ^{164}Dy and applying a background subtraction. Plot (b) shows the HPGe spectrum after gating on the yrast $4^+ \rightarrow 2^+$ transition at 177 keV in ^{166}Dy and applying a background subtraction. Plot (c) shows the HPGe spectrum after gating on the $(2_2^+) \rightarrow 0^+_{g.s.}$ transition at 857 keV in ^{166}Dy and applying a background subtraction. Plot (d) shows the HPGe spectrum after gating on the $(4^-) \rightarrow (3^+)$ transition at 252 keV in ^{166}Dy and applying a background subtraction. All background subtractions were performed by subtracting a background-gated HPGe projection from the peak-gated HPGe projection. The normalization factor used for the background subtraction was determined using the relative intensity of the 237 keV peak, which corresponds to the yrast $4^+ \rightarrow 2^+$ transition in ^{178}W. The difference in production cross section between the Coulomb excitation and $2n$ transfer reactions is clear from the reduction in γ-ray intensity originating from ^{166}Dy.

III. LEVEL SCHEME FOR ^{166}Dy OBSERVED IN THE CURRENT WORK

Observed transitions between the excited states populated in ^{166}Dy via the ^{164}Dy(^{18}O, ^{16}O) ^{166}Dy reaction are shown in the partial level scheme in Fig. 4. The data from a 76 MeV beam was sorted into a prompt HPGe-HPGe coincidence matrix, with a coincidence time window of 100 ns. Background-subtracted HPGe gates were set on various transitions within ^{166}Dy to complete the level scheme with the excited states

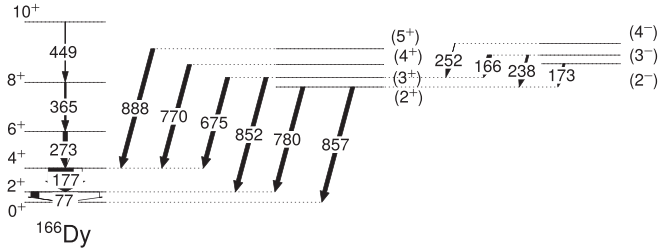

FIG. 4. Level scheme of ^{166}Dy from the γ-ray transitions observed in the current work following the ^{164}Dy(^{18}O, ^{16}O) ^{166}Dy reaction. The relative γ-ray intensities are taken from the 76 MeV beam energy data.

populated and γ-ray transitions seen in the current work. Details on the observed transitions and their intensities are given in Table I. The relative intensities were calculated by measuring the integrals of the γ rays in coincidence with the 177 keV yrast $4^+ \rightarrow 2^+$ transition and assuming 100% intensity for the 273 keV yrast $6^+ \rightarrow 4^+$ transition. In the current work, the yrast states up to the previously identified 10^+ state at 1341 keV (which depopulates via the 449 keV transition) [9] are observed [see Fig. 3(b)]. Higher-spin states such as the yrast $I^\pi = 12^+$ at 1868 keV or the 14^+ at 2467 keV, reported by Wu *et al.* [9], which depopulate via the 527 and 599 keV transitions respectively were not observed. This suggests an angular momentum population limit in the (^{18}O, ^{16}O) reaction mechanism.

TABLE I. The observed transitions associated with ^{166}Dy in the current work. Gamma ray energies, and spins and parities, where assigned, are taken from Ref. [22]. The total internal coefficients α_T are obtained from BRICC [23], for $\alpha_T > 0.02$. The relative intensities, I_γ(Rel.), are calculated for the data taken at a beam energy of 76 MeV, looking at the γ rays coincident with a 177 keV HPGe gate and assuming 100% intensity for the 273 keV transition. The total intensity, $I_{\text{Tot.}}$, is calculated as $I_\gamma(1+\alpha_T)$. The uncertainty on the γ-ray energies is 0.1 keV unless stated otherwise.

E_γ	I_γ(Rel.)	$I_{\text{Tot.}}$	J_i^π	J_f^π	α_{ICC}	Transition $E_i \rightarrow E_f$
76.6	34(2)	287(15)	2^+	0^+	7.51(11)	$77 \rightarrow 0$
166.5			(3^-)	$(3)^+$	0.0790(11)	$1095 \rightarrow 929$
172.7			(2^-)	$(2)^+$	0.0716(10)	$1030 \rightarrow 857$
176.9			4^+	2^+	0.357(5)	$254 \rightarrow 77$
238.1			(3^-)	$(2)^+$	0.0309(5)	$1095 \rightarrow 857$
252.1	13(1)	13(1)	(4^-)	$(3)^+$	0.0267(4)	$1181 \rightarrow 929$
273.4	100(5)	109(6)	6^+	4^+	0.0859(12)	$527 \rightarrow 254$
365(1)	28(2)	29(2)	8^+	6^+	0.0360(5)	$892 \rightarrow 527$
449(1)	12(1)	12(1)	10^+	8^+	0.0202(3)	$1341 \rightarrow 892$
675.2	16(1)	16(1)	$(3)^+$	4^+		$929 \rightarrow 254$
769.9	43(2)	43(2)	$(4)^+$	4^+		$1023 \rightarrow 254$
780.6			$(2)^+$	2^+		$857 \rightarrow 77$
852.1			$(3)^+$	2^+		$929 \rightarrow 77$
857.2			$(2)^+$	0^+		$857 \rightarrow 0$
887.7	27(2)	27(2)	(5^+)	4^+		$1141 \rightarrow 254$

Excited states in ^{166}Dy have been reported previously, following population via ^{166}Tb β^- decay [11], the ^{164}Dy(t, p) reaction [10], and successive thermal neutron capture on ^{165}Dy [22,24]. The current work clearly identifies coincident γ rays at energies of 675, 770, and 888 keV; see Figs. 4 and 3(b). These correspond to de-excitations from previously identified states [25] in the nominal $K = 2$ γ band with spin-parity values (3^+), (4^+), and (5^+), and excitation energies of 929, 1023, and 1141 keV respectively. The coincident 252 keV transition has also been reported previously as depopulating the $I^\pi = 4^-$, $K^\pi = 2^-$ two-quasi-particle state with excitation energy 1181 keV [25]; this is clearly observed in the current work [see Figs. 4 and 3(d)]. No evidence was observed in the current work for any delayed, out of beam component for the 252 keV $4^- \rightarrow 3^+$ $E1$ transition in ^{166}Dy, consistent with a small change in K value.

IV. LIFETIME MEASUREMENT TECHNIQUES

To measure the excited state lifetimes in Dy isotopes the fast timing technique [26,27] was implemented. This γ-ray coincidence method takes advantage of the excellent timing resolution available in the $LaBr_3$ scintillators. A time difference distribution is obtained by sampling the time difference between the detection of the γ rays populating (*feeding*) and depopulating (*decaying*) the excited state. From the analyses, a HPGe-gated E-E-ΔT cube is produced, enabling $LaBr_3$ energy gates to be set on the *decay* E_d and *feeder* E_f transitions to create the ΔT distribution. The ΔT distribution, produced by N_0 pairs of γ rays feeding and decaying from an excited state, can be described by a convolution of the prompt response function (PRF) and an exponential decay due to the mean lifetime, τ, of the state, such as in Refs. [26,28]:

$$D(t) = \frac{1}{\tau} N_0 \int_{-\text{inf}}^{t} \text{PRF}(t') e^{\frac{t-t'}{\tau}} dt'. \tag{1}$$

For cases where $\tau \gtrsim$ FWHM, the mean lifetime can be obtained by fitting the slope of the exponential decay in the time distribution [21]. If $\tau <$ FWHM, the lifetime can be measured using the generalized centroid difference (or centroid shift) method [28–30]. To use this method, the prompt response curve (PRC), which describes the energy-dependent time walk of the setup, must be obtained [31]. The PRC calibration was performed using a ^{152}Eu source and taking the 344 keV $2^+ \rightarrow 0^+$ transition of ^{152}Gd as the reference energy; the obtained PRC is shown in Fig. 5. The shift of the centroid of the time difference distribution $\Delta C(D(t))$ of the measured *feeder* and *decay* transitions can then be compared with the PRC to obtain the lifetime of the state:

$$\Delta C = C(E_d, E_f) = \text{PRC}(E_d, E_f) + \tau, \tag{2}$$

where $C(E_d, E_f)$ is the centroid of the time difference distribution $\Delta T = T(E_{\text{decay}}) - T(E_{\text{feeder}})$, and $\text{PRC}(E_d, E_f) = \text{PRC}(E_f) - \text{PRC}(E_d)$.

When using the centroid shift method, corrections for the background present in the $LaBr_3$ energy gates have to be applied, using the correction method described in Ref. [32],

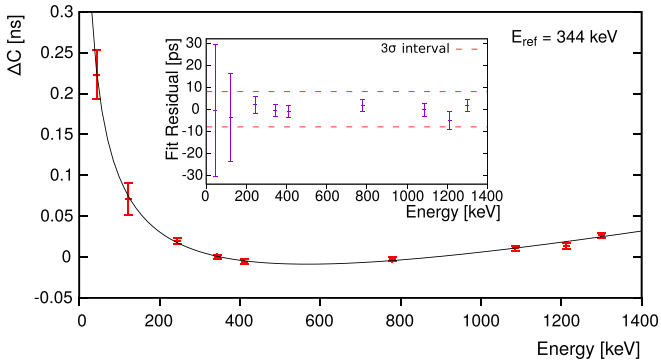

FIG. 5. The PRC with reference energy $E_{\rm ref} = 344$ keV. The deviation of the data points from this curve is shown in the inset, and the 3σ interval of 8 ps is taken as the uncertainty of the PRC.

where,

$$C^t_{PP} = \frac{n_{PP}C_{PP} - n_{PB}C_{PB} - n_{BP}C_{BP} + n_{BB}C_{BB}}{n_{PP} - n_{PB} - n_{BP} + n_{BB}}, \qquad (3)$$

where C^t_{PP} is the true position of the centroid, after correcting the measured centroid C_{PP} for the centroids of the background time distributions: C_{PB}, C_{BP}, and C_{BB}. The corrections were weighted according to the integrals of these background time distributions: n_{PB}, n_{BP}, and n_{BB} respectively. In this notation PP refers to ΔT(peak, peak) and PB refers to ΔT(peak, background), to indicate whether the $LaBr_3$ energy gate was set on the *feeder*/*decay* peak or on a neighboring background region.

V. LIFETIME ANALYSES

To maximize the available statistics and reduce uncertainties on the obtained lifetimes, the data acquired at all three beam energies was summed together for the lifetime analyses. First, the results for the ^{164}Dy lifetime measurements will be presented, followed by the half-life measurement for the first 2^+ excited state in the ^{166}Dy nucleus.

A. ^{164}Dy

The channel selection of ^{164}Dy and lifetime measurements in this nucleus form a proof-of-principle analysis which verify the quality of the dataset. Triple coincident HPGe-$LaBr_3$-$LaBr_3$ events were selected, where the HPGe γ ray was prompt ($\pm$50 ns of the beam pulse) and the $LaBr_3$ γ rays were both prompt ($\pm$17 ns of the beam pulse). Coincident events in the $LaBr_3$ detectors were vetoed if a nearest-neighbor detector fired within the coincidence time window, which was in essence an active Compton suppression condition. A HPGe gate was set on a discrete γ ray from within the yrast band, and two $LaBr_3$ energy gates were set subsequently on the transitions required to obtain the time difference distribution to establish the excited state lifetime. The purity of the $LaBr_3$ gates was verified by HPGe-HPGe and HPGe-$LaBr_3$-HPGe gates on the data.

A HPGe gate was set on the $6^+ \rightarrow 4^+$ transition of ^{164}Dy at 259 keV, to enable a clean $LaBr_3$-$LaBr_3$ time difference to be obtained between the 169 keV $4^+ \rightarrow 2^+$ and 73 keV $2^+ \rightarrow 0^+$ transitions. Figure 6(a) shows the $LaBr_3$ projection from the background-subtracted, 259 keV HPGe-gated E-E-ΔT cube. The $LaBr_3$ projections after setting $LaBr_3$ energy gates on the 73 and 169 keV transitions are shown in Figs. 6(b) and 6(c).

The resulting $\Delta T(73, 169)$ time distribution is shown in Fig. 7; an exponential decay and constant background are fitted simultaneously. The half-life obtained is 2.35(6) ns, in good agreement with the literature value of 2.393(29) ns [33,34].

The lifetime of the first 4^+ excited state was measured using the centroid shift technique. A HPGe gate was set on the $8^+ \rightarrow 6^+$ transition of ^{164}Dy at 342 keV [see Figs. 6(d)–6(f)]. Two-dimensional (2D) background/random gates were set at energies above and below the 169 and 259 keV transitions, as shown in Fig. 8(a). The values for the centroids and integrals were calculated as an average of the two distributions created using the background above and below the peak.

The $\Delta T(169, 259)$ time distribution is shown in Fig. 8(b) with the three background time distributions which were used for the correction. For simplicity, only the time spectra corresponding to regions $P|B_1$, $B|P_1$, and $B|B_1$ are plotted. Using Eq. (3) the background-corrected value for the centroid was calculated as 0.243(7) ns. This centroid was then corrected for the $LaBr_3$ time walk using the PRC shown in Fig. 5 to obtain the lifetime of the yrast 4^+ state in ^{164}Dy of $\tau(^{164}\text{Dy}, 4^+_1) = 0.273(10)$ ns [$T_{1/2} = 0.189(7)$ ns], which compares with the literature value of $T_{1/2} = 0.201(8)$ ns [33,35].

For the 6^+ yrast state in ^{164}Dy, the E-E-ΔT cube was constructed with a HPGe gate on the $4^+ \rightarrow 2^+$ transition at 169 keV. Figure 8(c) shows where the 2D $LaBr_3$ gates were set to produce the four time distributions. Again, the centroids and integrals of three background time distributions were calculated as averages from the gates above and below the 259 and 342 keV transitions. The $\Delta T(259, 342)$ distribution is shown in Fig. 8(d), with the three background component time distributions when using the background gates below the peaks. The background-corrected value for the centroid was 0.019(4) ns. The additional correction for the PRC then gave $\tau(^{164}\text{Dy}, 6^+_1) = 0.031(8)$ ns, corresponding to $T_{1/2} = 22(6)$ ps, consistent with the literature value of 27.2(8) ps [33,35].

B. ^{166}Dy

For the optimal selection of the ^{166}Dy nucleus, for timing gates, it was useful to use a combination of HPGe gating with a total event multiplicity constraint. Gated E-E-ΔT cubes were produced with a HPGe gate on either the yrast $6^+ \rightarrow 4^+$ or the $4^+ \rightarrow 2^+$ transition in ^{166}Dy, and only the events with a total multiplicity of $N \leqslant 4$ were used. Figures 9(a) and 9(d) show the $LaBr_3$ projections from the E-E-ΔT cubes with HPGe gates on 273 and 177 keV, respectively. The $LaBr_3$ projections after setting $LaBr_3$ energy gates on the 77 and 177 keV transitions and on the 77 and 273 keV transitions are shown in Figs. 9(b), 9(c), 9(e), and 9(f) respectively.

The similarities of low-lying levels in ^{164}Dy and ^{166}Dy, and the fact that $T_{1/2}(^{164}\text{Dy}, 4^+_1) \ll T_{1/2}(^{164}\text{Dy}, 2^+_1)$, suggests that the exponential decay of the 4^+_1 in ^{166}Dy is short

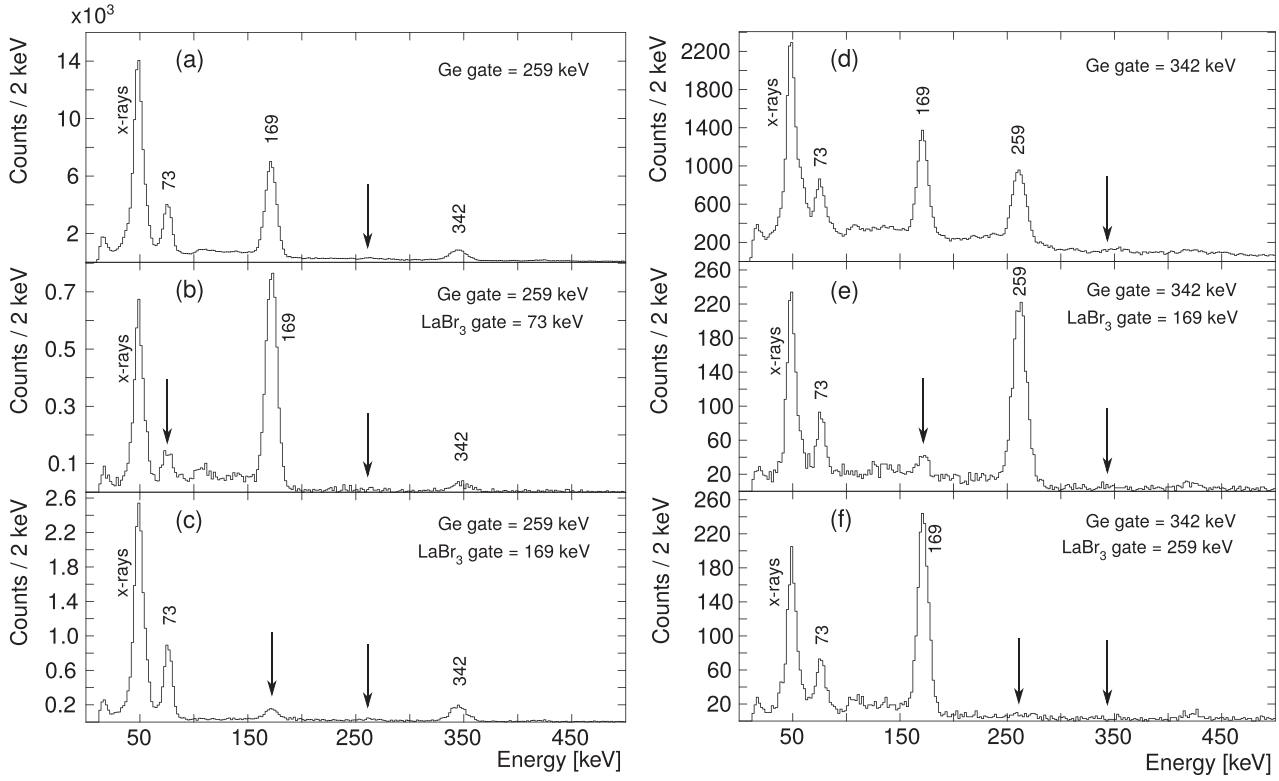

FIG. 6. Gamma-ray coincidence spectra for transitions in ^{164}Dy. (a)–(c) HPGe-gated, $LaBr_3$ projected γ-ray spectra to demonstrate the selectivity of the $LaBr_3$ gates used for $\Delta T(73, 169)$. (d)–(f) HPGe-gated, $LaBr_3$ projected γ-ray spectra used for $\Delta T(169, 259)$. Arrows indicate the energies where gates were set. Note that there are still peaks present at 169 and 73 keV even when this is the gate energy due to Compton coincidences. These plots were produced using combined data from all three beam energies.

enough to not significantly affect the decay curve of the 2_1^+ state. The time differences $\Delta T(77, 177)$ and $\Delta T(77, 273)$ are summed and fitted with an exponential decay plus a constant background, as shown in Fig. 10. The obtained half-life value is 2.3(2) ns.

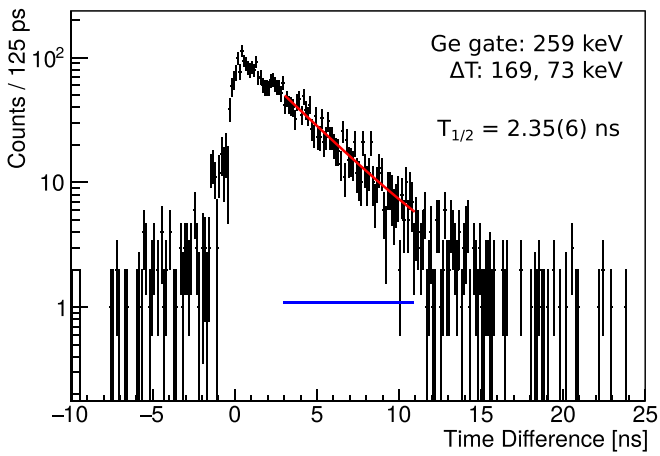

FIG. 7. Time distribution for the yrast 2^+ state in ^{164}Dy, obtained using gates on the decay energy $E_d = 73$ keV and feeding energy $E_f = 169$ keV. The deduced half-life is given in the legend.

VI. RESULTS AND DISCUSSIONS

The reduced transition probability $B(E2)\downarrow$ is related to the lifetime of the excited state by [36]

$$B(E2)\downarrow = \frac{1}{\tau(1+\alpha_T)\times 1.225\times 10^{13}\times E_\gamma^5} \tag{4}$$

to give $B(E2)\downarrow$ in e^2b^2, where τ is the neutral atom mean lifetime in seconds, E_γ is the stretched $E2$ transition energy in MeV, and α_T is the total internal conversion coefficient. The relationship between the intrinsic quadrupole moment Q_0 and the reduced transition probability is given by [36]

$$B(E2)\downarrow = \frac{5}{16\pi}Q_0^2|\langle IK20|(I-2)K\rangle|^2 \tag{5}$$

where $\langle IK20|I-2K\rangle$ is the Clebsch-Gordan coefficient for an initial nuclear spin of I, a nuclear spin of $I-2$ following the decay, and a projection of the intrinsic angular momentum on the symmetry axis of K. Equation (5) applies for $E2$ transitions within a rotational band and gives Q_0 in eb. If the nucleus is an even-even nucleus then it is assumed that $K = 0$ [37]. Finally, the β_2 deformation parameter can be calculated using the expression [38]

$$Q_0 = \sqrt{\frac{16\pi}{5}}\frac{3}{4\pi}ZeR_0^2\beta_2, \tag{6}$$

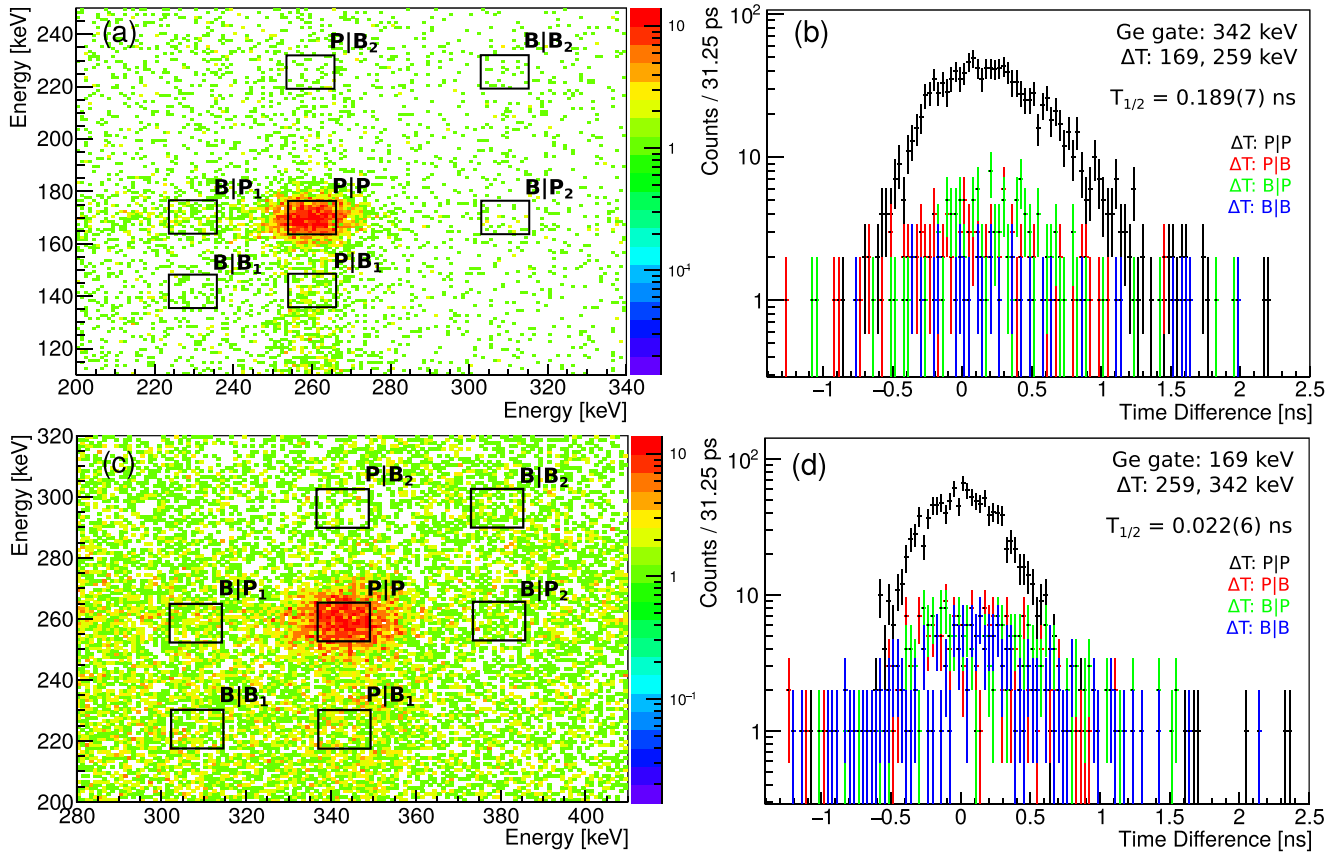

FIG. 8. (a) 2D projection of the E-E-ΔT cube showing the coincidence peak at 169-259 keV, and the six background regions used to correct the ΔT centroid. (b) Time distribution for $T_{1/2}(^{164}\text{Dy}, 4_1^+)$ with the decay energy $E_d = 169$ keV and feeding energy $E_f = 259$ keV. (c) 2D projection of the E-E-ΔT cube showing the coincidence peak at 259-342 keV, and the three background regions used to correct the ΔT centroid. (d) Time distribution for $T_{1/2}(^{164}\text{Dy}, 6_1^+)$ with the decay energy $E_d = 259$ keV and feeding energy $E_f = 342$ keV. These plots were produced using combined data from all three beam energies.

where Ze is the nuclear charge and $R_0 = 1.2A^{1/3}$ fm is the nuclear radius. Uncertainties on $B(E2)\downarrow$, Q_0 and β_2 are calculated by propagating through the uncertainty on the measured mean lifetime τ.

For the ^{164}Dy nucleus, Table II gives the lifetime results and corresponding $B(E2)\downarrow$ and Q_0 values calculated in this work.

For the ^{166}Dy nucleus, the lifetime for the 2_1^+ state obtained in the current work and its corresponding $B(E2)\downarrow$ and β_2 values are given in Table III. The values are compared with those of the other even-even Dy isotopes, for $94 \leqslant N \leqslant 100$. For ^{164}Dy the values obtained in this work are used.

The systematic trends of the $B(E2\downarrow)$ values for even-even nuclei between $64 \leqslant Z \leqslant 70$ and $94 \leqslant N \leqslant 104$ are shown in Fig. 11. As expected, there is an increasing trend in the $B(E2)\downarrow$ as N approaches $N = 104$ for all of these nuclei, but $E(2_1^+, {}^{164}\text{Dy}) < E(2_1^+, {}^{166}\text{Dy})$ implies that the maximum quadrupole deformation occurs at $N = 98$ for Dy isotopes.

TABLE II. A summary of the measured $T_{1/2}$ and $B(E2)\downarrow$ values for ^{164}Dy. Excitation energy, E_{ex}, is given in keV, $T_{1/2}$ is given in ns, $B(E2)\downarrow$ is given in $e^2\text{b}^2$, Q_0 is given in eb, and (LIT.) refers to the evaluated literature values [33].

J^π	E_{ex}	$T_{1/2}$	$T_{1/2}$ (LIT.)	$B(E2)\downarrow$	Q_0
2^+	73.393(5)	2.35(6)	2.393(29)	1.14(3)	7.58(9)
4^+	242.234(7)	0.189(7)	0.201(8)	1.54(6)	7.35(14)
6^+	501.330(12)	0.022(6)	0.0272(8)	2.0(5)	8.0(11)

TABLE III. A summary of the measured $T_{1/2}$ and $B(E2)\downarrow$ values for different Dy isotopes. $T_{1/2}$ is given in ns and $B(E2)\downarrow$ is given in $e^2\text{b}^2$ [33]. The values for the total internal conversion coefficient α_T were obtained from BRICC [23]. Nuclear data for the ^{160}Dy and ^{162}Dy nuclei are taken from Refs. [40] and [41], respectively.

Nucleus	$E(2^+)$	$T_{1/2}(2^+)$	α_{ICC}	$B(E2)\downarrow$	β_2
^{160}Dy	86.78	2.02(1)	4.63	1.011(5)	0.3361(8)
^{162}Dy	80.66	2.19(2)	6.14	1.060(10)	0.3414(16)
^{164}Dy	73.39	2.35(6)	8.890	1.14(3)	0.352(4)
^{166}Dy	76.7	2.3(2)	7.480	1.12(11)	0.345(17)

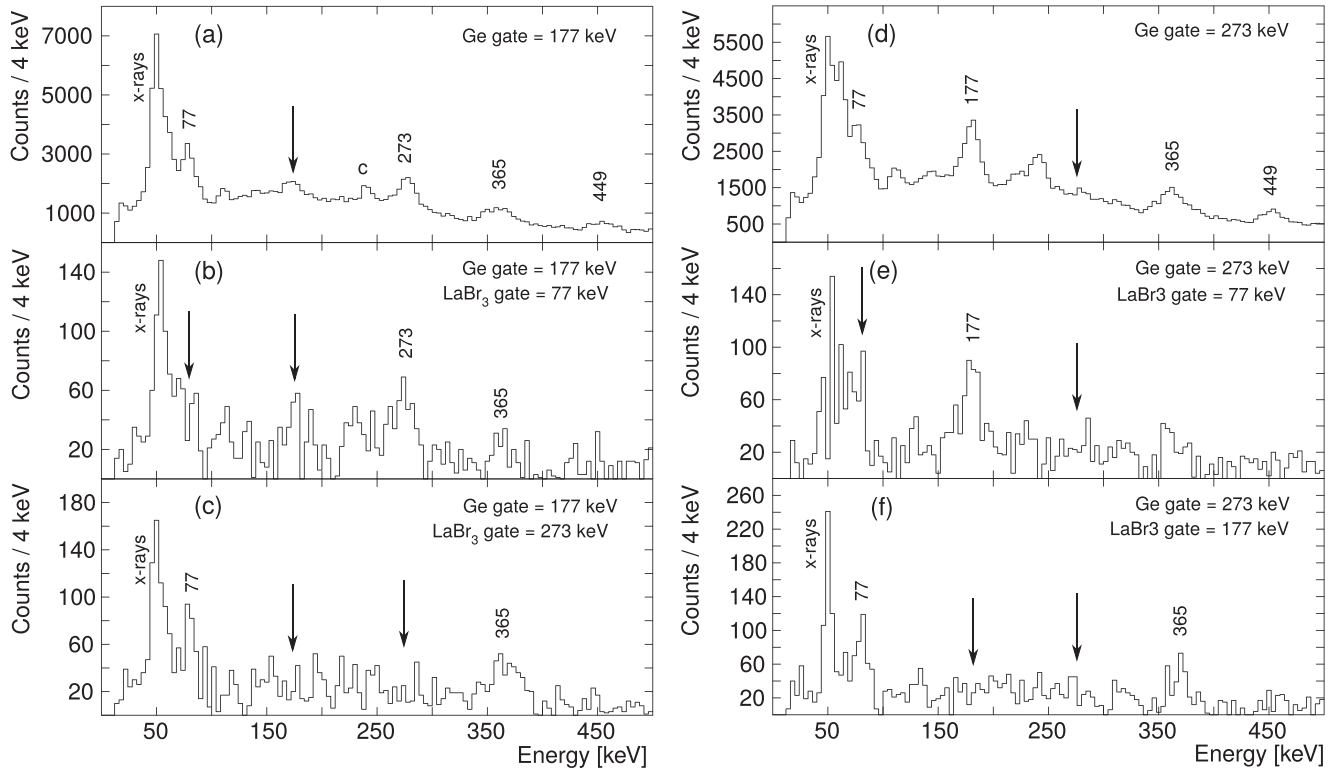

FIG. 9. Gamma-ray coincidence spectra for transitions in ^{166}Dy. (a)–(c) HPGe-gated, $LaBr_3$ projected γ-ray spectra demonstrating the selectivity of the $LaBr_3$ energy gates used for $\Delta T(77, 177)$. (d)–(f) HPGe-gated, $LaBr_3$ projected γ-ray spectra used for $\Delta T(77, 273)$. The peak labeled "c" corresponds to a weak contamination from the 237 keV yrast $4^+ \rightarrow 2^+$ transition in ^{178}W, which is the strongest line in the total projection. These plots were produced using combined data from all three beam energies.

The value for $B(E2)\downarrow$ in ^{164}Dy obtained in the current work is clearly compatible with the value calculated from [33].

Relativistic mean-field calculations by Lalazissis *et al.* [47] predict an increasing β_2 deformation for the Dy isotopes towards the $N = 104$ mid-shell, but with a near saturation of collective behavior and deformation from $N = 98$ (^{164}Dy).

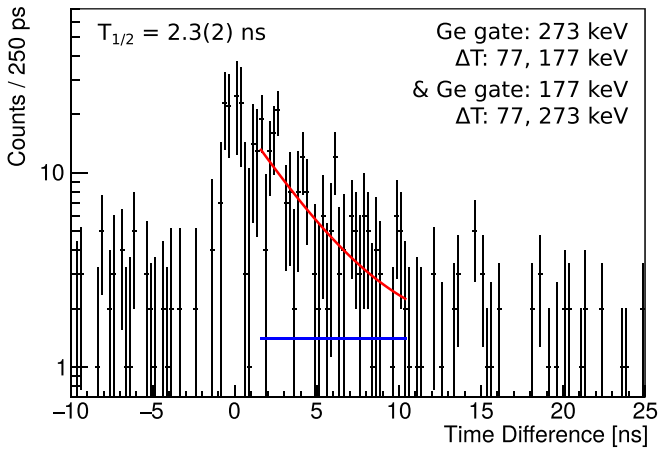

FIG. 10. Time distribution for the yrast 2^+ state in ^{166}Dy, obtained using gates on the decay energy $E_d = 77$ keV and feeding energy $E_f = 177$ keV or $E_f = 273$ keV. The deduced half-life from the fit is given in the legend.

More recent work by Bonatsos *et al.* uses the proxy-SU(3) scheme to make predictions of the β (and γ) deformation variable for the Dy isotopes, with increasing N [48]. The Dy deformations are predicted to be among the largest in the region and to saturate at a value of $\beta \simeq 0.3$ between $N = 98$ and $N = 102$.

Self-consistent density-dependent Hartree-Fock calculations with BCS pairing were reported by Rath *et al.* [7],

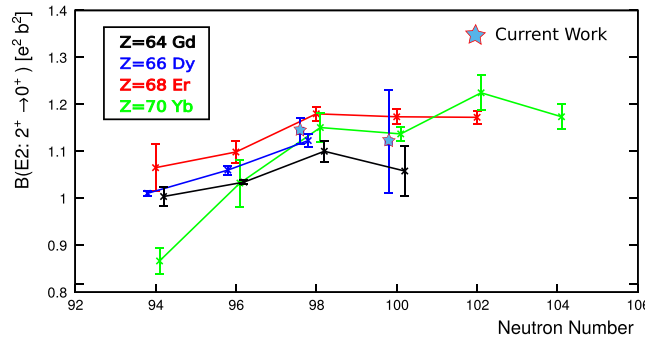

FIG. 11. Systematics of $B(E2)\downarrow$ for Gd, Dy, Er, and Yb isotopes with $94 \leqslant N \leqslant 104$; data taken from [22,33,39–46]. The $B(E2)\downarrow$ values for ^{164}Dy and ^{166}Dy calculated here are added as starred data points. The isotopes are slightly offset at each value of N to allow each data point and error bar to be seen.

which also predict a saturation of β_2 at ≈0.35 in the range $A = 162$–170 ($N = 96$–104) across the Dy isotopic chain. While the energy systematics of the 2^+ yrast states suggest a deformation maxima at $N = 98$ (local) and possibly $N = 104$ (global) [12], the current work is consistent with the predicted deformation saturation. This is also the first direct $B(E2)$ measurement in a neutron-rich Dy isotope and provides a bridge for future higher-precision studies towards and across the $N = 104$ mid-shell valence maximum, possibly following production via high-energy projectile fission reactions as studied in [13–15].

ACKNOWLEDGMENTS

The authors would like to thank the operators of the ALTO facility for providing the reliable beams used during the experiment. Additionally we thank the FASTER collaboration for the technical support given. GAMMA-POOL and LOAN-POOL are acknowledged for loaning the Clover and Phase I HPGe detectors. The FATIMA Collaboration is acknowledged for loaning the LaB_3 detectors. This work was supported by the STFC UK Nuclear Data Network, the STFC (Grants No. ST/L005743/1 and No. ST/P005314), the Marion Redfearn Trust, BMBF (NUSTAR.DA Grant No. 05P15RDFN1), and Spanish MINECO Grant No. FPA2015-65035-P. The research leading to these results has received funding from the European Union's HORIZON2020 Program under Grant Agreement No. 654002. P.H.R., S.M.C., G.L., and R.S. acknowledge support from the UK Department of Business, Energy and Industrial Strategy (BEIS) via the National Measurement System and from the STFC consolidated grant.

APPENDIX: A NOTE ON UNCERTAINTY CALCULATIONS

Error bars on the statistics in each channel are always taken into account in the total uncertainty on a lifetime result, these are assumed to be the square root of the number of counts in each channel. Where cubes or histograms were added together or subtracted from one another, these error bars were propagated by summing in quadrature.

Factors taken into account for the uncertainty determination when using the decay slope fit were the following: the statistical uncertainty on the number of counts in each bin i, δn_i; the uncertainty of the binned likelihood fit, δ fit, given by the fit residuals at the 1σ interval; and the uncertainty on the decay constant parameter due to variation of the constant background parameter, $\delta\lambda(bg)$, given by the distribution in λ at the 1σ interval. The standard uncertainty of the half-life was derived by adapting the methodology described in Ref. [49].

For the centroid shift method, the uncertainty on the background corrected centroid is given by

$$\delta C^t_{PP} = \sqrt{\sum_i \left(\left| \frac{\partial C^t_{PP}}{\partial n_i} \right| \delta n_i \right)^2 + \sum_i \left(\left| \frac{\partial C^t_{PP}}{\partial C_i} \right| \delta C_i \right)^2}, \quad \text{(A1)}$$

where i represents the three background regions $P|B$, $B|P$, and $B|B$, such that δC_i and δn_i are the uncertainties on the centroids and integrals of the three background regions respectively. δC^t_{PP} was added in quadrature with the uncertainty $\delta\,\mathrm{PRC} = 0.008$ ns from the PRC correction, to give the overall uncertainty on τ:

$$\delta\tau = \sqrt{\left(\delta C^t_{PP}\right)^2 + \left(\delta\,\mathrm{PRC}\right)^2} \quad \text{(A2)}$$

[1] N. V. Zamfir, R. F. Casten, and D. S. Brenner, Phys. Rev. Lett. **72**, 3480 (1994).
[2] R. F. Casten, K. Heyde, and A. Wolf, Phys. Lett. B **208**, 33 (1988).
[3] R. F. Casten, P. von Brentano, and A. M. I. Haque, Phys. Rev. C **31**, 1991 (1985).
[4] P. H. Regan, F. R. Xu, P. M. Walker, M. Oi, A. K. Rath, and P. D. Stevenson, Phys. Rev. C **65**, 037302 (2002).
[5] Z. Patel *et al.*, Phys. Rev. Lett. **113**, 262502 (2014).
[6] S. K. Ghorui, B. B. Sahu, C. R. Praharaj, and S. K. Patra, Phys. Rev. C **85**, 064327 (2012).
[7] A. K. Rath, P. D. Stevenson, P. H. Regan, F. R. Xu, and P. M. Walker, Phys. Rev. C **68**, 044315 (2003).
[8] C. E. Vargas, V. Verlázquez, and S. Lerma, Eur. Phys. J. A **49**, 4 (2013).
[9] C. Y. Wu, M. W. Simon, D. Cline, G. A. Davis, A. O. Macchiavelli, and K. Vetter, Phys. Rev. C **57**, 3466 (1998).
[10] D. G. Burke, G. Løvhøiden, and T. F. Thorsteinsen, Nucl. Phys. A **483**, 221 (1988).
[11] S. Ichikawa *et al.*, Nucl. Instrum. Methods Phys. Res., Sect. A **374**, 330 (1996).
[12] P.-A. Söderström *et al.*, Phys. Rev. C **81**, 034310 (2010).
[13] G. X. Zhang *et al.*, Phys. Lett. B **799**, 135036 (2019).
[14] P.-A. Söderström *et al.*, Phys. Lett. B **762**, 404 (2016).
[15] H. Watanabe *et al.*, Phys. Lett. B **760**, 641 (2016).
[16] S. V. Smith, N. D. Bartolo, S. Mirzadeh, R. M. Lambrecht, F. F. Knapp, Jr., and E. L. Hetherington, Appl. Radiat. Isot. **46**, 759 (1995).
[17] P. E. Edem, J. Fonslet, A. Kjær, M. Herth, and G. Severin, Bioinorg. Chem. Appl. **2016**, 6148357 (2016).
[18] M. Rudigier *et al.*, Phys. Lett. B **801**, 135140 (2020).
[19] M. Lebois, N. Jovancevic, J. N. Wilson, D. Thisse, R. L. Canavan, and M. Rudigier, Acta Phys. Pol. B **50**, 425 (2019).
[20] N. Jovančević *et al.*, Acta Phys. Pol. B **50**, 297 (2019).
[21] M. Rudigier *et al.*, Acta Phys. Pol. B **50**, 661 (2019).
[22] C. M. Baglin, Nucl. Data Sheets **109**, 1103 (2008).
[23] T. Kibédi, T. W. Burrows, M. B. Trzhaskovskaya, P. M. Davidson, and C. W. Nestor, Jr., Nucl. Instrum. Methods Phys. Res., Sect. A **589**, 202 (2008).
[24] E. Kaerts and P. H. M. Van Assche, Nucl. Phys. A **514**, 173 (1990).
[25] E. Kaerts, L. Jacobs, G. Vandenput, and P. H. M. Van Assche, Nucl. Instrum. Methods Phys. Res., Sect. A **267**, 473 (1988).
[26] J.-M. Régis, M. Dannhoff, and J. Jolie, Nucl. Instrum. Methods Phys. Res., Sect. A **897**, 38 (2018).
[27] J.-M. Régis, M. Dannhoff, J. Jolie, C. Müller-Gatermann, and N. Saed-Samii, Nucl. Instrum. Methods Phys. Res., Sect. A **811**, 42 (2016).

[28] J.-M. Régis and H. Mach, Nucl. Instrum. Methods Phys. Res., Sect. A **726**, 191 (2013).
[29] J.-M. Régis, G. Pascovici, J. Jolie, and M. Rudigier, Nucl. Instrum. Methods Phys. Res., Sect. A **622**, 83 (2001).
[30] J.-M. Régis *et al.*, Nucl. Instrum. Methods Phys. Res., Sect. A **823**, 72 (2016).
[31] J.-M. Régis, M. Rudigier, J. Jolie, A. Blahzev, C. Fransen, G. Pascovici, and N. Warr, Nucl. Instrum. Methods Phys. Res., Sect. A **684**, 36 (2012).
[32] E. R. Gamba, A. M. Bruce, and M. Rudigier, Nucl. Instrum. Methods Phys. Res., Sect. A **928**, 93 (2019).
[33] B. Singh and J. Chen, Nucl. Data Sheets **147**, 1 (2018)
[34] R. Avida, Y. Dar, P. Gilad, M. B. Goldberg, K. H. Speidel, and Y. Wolfson, Nucl. Phys. A **127**, 412 (1969).
[35] S. H. Sie and D. W. Gebbie, Nucl. Phys. A **289**, 217 (1977).
[36] A. Bohr and B. R. Mottelson, *Nuclear Structure*: Vol. 1 (World Scientific, Singapore, 1969).
[37] A. Bohr, B. R. Mottelson, *Nuclear Structure*: Vol. 2 (World Scientific, Singapore, 1975).
[38] A. G. Smith, J. L. Durell, W. R. Phillips, W. Urban, P. Sarriguren, and I. Ahmad, Phys. Rev. C **86**, 014321 (2012).
[39] N. Nica, Nucl. Data Sheets **141**, 1 (2017).
[40] C. W. Reich, Nucl. Data Sheets **105**, 557 (2005).
[41] C. W. Reich, Nucl. Data Sheets **108**, 1807 (2007).
[42] C. M. Baglin, Nucl. Data Sheets **111**, 1807 (2010).
[43] C. M. Baglin, E. A. McCutchan, S. Basunia, and E. Browne, Nucl. Data Sheets **153**, 1 (2018).
[44] B. Singh, Nucl. Data Sheets **75**, 199 (1995).
[45] E. Browne and H. Junde, Nucl. Data Sheets **87**, 15 (1999).
[46] B. Pritychenko, M. Birch, and B. Singh, Nucl. Phys. A **962**, 73 (2017).
[47] G. A. Lalazissis, M. M. Sharma, and P. Ring, Nucl. Phys. A **597**, 35 (1996).
[48] D. Bonatsos, I. E. Assimakis, N. Minkov, A. Martinou, R. B. Cakirli, R. F. Casten, and K. Blaum, Phys. Rev. C **95**, 064325 (2017).
[49] S. Pommé, Metrologia **52**, S51 (2015).